

Article

# The Morphologically Controlled Synthesis and Application of Mesoporous Alumina Spheres

Yadian Xie <sup>1,\*</sup>, Lanxing Gao <sup>1,†</sup>, Miaoxuan Xue <sup>1,†</sup>, Yanqing Hou <sup>1,2</sup>, Bo Yang <sup>1,2</sup>, Lingyun Zhou <sup>1,\*</sup> and Xin Tong <sup>1,3,\*</sup> 

- <sup>1</sup> Guizhou Provincial Key Laboratory in Higher Education Institutions of Low-Dimensional Materials and Environmental and Ecological Governance, Key Laboratory of Low-Dimensional Materials and Big Data, College of Chemical Engineering, Guizhou Minzu University, Guiyang 550025, China; glxprettylife@163.com (L.G.); xuemx0418@163.com (M.X.); hhoyanqing@163.com (Y.H.); gznuyangbo@163.com (B.Y.)
- <sup>2</sup> Faculty of Metallurgy and Energy Engineering, Kunming University of Science and Technology, Kunming 650093, China
- <sup>3</sup> School of Chemistry and Material Science, Guizhou Normal University, Guiyang 550001, China
- \* Correspondence: xieyadian@gzmu.edu.cn (Y.X.); zhoulingyun201508@163.com (L.Z.); tongxin@gznu.edu.cn (X.T.)
- † These authors contributed equally to this work.

**Abstract:** The control of alumina morphology is crucial yet challenging for its various applications. Unfortunately, traditional methods for preparing alumina particles suffer from several limitations such as irregular morphology, poor dispersibility, and restricted application areas. In this study, we develop a novel method for preparing spherical mesoporous alumina using chitin and Pluronic P123 as mixed templates. The effects of reaction temperature, time, and the addition of mixed templates on the phase structure, micromorphology, and optical absorption properties of the samples were investigated. The experimental results indicate that lower temperature and shorter reaction time facilitated the formation of spherical mesoporous alumina with excellent CO<sub>2</sub> adsorption capacity. The periodic density functional theory (DFT) calculations demonstrate that both the (110) and (100) surfaces of  $\gamma$ -Al<sub>2</sub>O<sub>3</sub> can strongly adsorb CO<sub>2</sub>. The difference in the amount of CO<sub>2</sub> adsorbed by Al<sub>2</sub>O<sub>3</sub> is mainly due to the different surface areas, which give different numbers of exposed active sites. This approach introduces a novel strategy for utilizing biological compounds to synthesize spherical alumina and greatly enhances mesoporous alumina's application efficiency in adsorption fields. Moreover, this study explored the electrochemical performance of the synthesized product using cyclic voltammetry, and improved loading of electrocatalysts and enhanced electrocatalytic activity were discovered.

**Keywords:** mesoporous alumina; chitin; P123; hydrothermal method



**Citation:** Xie, Y.; Gao, L.; Xue, M.; Hou, Y.; Yang, B.; Zhou, L.; Tong, X. The Morphologically Controlled Synthesis and Application of Mesoporous Alumina Spheres.

*Molecules* **2023**, *28*, 5622.

<https://doi.org/10.3390/molecules28155622>

molecules28155622

Received: 4 July 2023

Revised: 21 July 2023

Accepted: 22 July 2023

Published: 25 July 2023



**Copyright:** © 2023 by the authors. Licensee MDPI, Basel, Switzerland. This article is an open access article distributed under the terms and conditions of the Creative Commons Attribution (CC BY) license (<https://creativecommons.org/licenses/by/4.0/>).

## 1. Introduction

In recent years, alumina has gained significant attention in high-value applications such as adsorbent [1–3], ceramic [4,5], catalyst and catalyst carrier [6–9] applications, etc. The application of alumina is not only dependent on particle size but also on particle shape. Different shapes of alumina, such as rod-like [10], fibrous [11], plate-like [12], and spherical [13] shapes, have been widely used. Seyed [14] obtained massive  $\gamma$ -aluminum with particle sizes between 0.5  $\mu$ m and 0.9  $\mu$ m, but the morphology was irregular. Dabbagh et al. and Feng et al. [15,16] prepared rod-like, fibrous, and spherical alumina, but the process was complex and hard to control, resulting in poor dispersibility. Lv et al. [17] synthesized spherical alumina with a highly spherical shape and uniform particle size by using the oil–ammonia drop method, but the particle size was large, which limited its application area. Using aluminum isopropoxide as a precursor and Pluronic P123 (P123) as a

template, Wu et al. [18] synthesized organized mesoporous alumina with a hierarchical structure. However, these methods suffer from limitations such as irregular morphology, poor dispersibility, and limited application areas.

Mesoporous materials are highly valued due to their higher specific surface area, organized pore structure, narrow pore size distribution, and continuous pore size, which make them important for adsorption and separation, as well as catalytic reactions [19–23]. Among various shapes of alumina, spherical alumina has high fluidity, making it less prone to gathering and producing channeling during catalytic processes, which significantly enhances catalyst activity. Therefore, the preparation of mesoporous alumina can greatly improve the application efficiency of mesoporous alumina spheres in adsorption, separation, and catalysis [24].

Chitin ((C<sub>8</sub>H<sub>13</sub>O<sub>5</sub>N)<sub>n</sub>) is a naturally occurring biopolymer that is highly organized and abundant in the exoskeletons of crustaceans and insects. The primary chitin fibrils' structural arrangement varies among arthropod species, with some having helical structures called the Bouligand structure, which enhances photonic and mechanical properties. This structure resembles cholesteric lyotropic liquid crystals. The hierarchical structure of chitin fibrils makes them an excellent natural template for developing new materials. The use of biomass as a porous material can achieve biodegradability, achieve biocompatibility, and achieve green and sustainable development [25–29]. Pluronic P123 (P123) is a soft template with a symmetric triblock copolymer comprising poly (ethylene oxide) (PEO) alternating with poly (propylene oxide) (PPO), PEO-PPO-PEO. Its phases vary depending on the concentration and combination of solvents [30–33] and it is often used as a crystal structure modifier in the preparation of mesoporous materials [34].

In this study, mesoporous alumina spheres were successfully prepared using alumina hydrate (AlOOH) as a precursor, (NH<sub>2</sub>)<sub>2</sub>CO as a precipitant, and chitin powder and P123. The preparation process, which involved evaporation-induced self-assembly (EISA), was green, low-cost, and pollution-free. This method significantly improved the catalyst loading firmness and service life of mesoporous alumina spheres. The effects of synthesis temperature, time, and the addition of mixed templates on the structure and morphology of the products were investigated. The CO<sub>2</sub> adsorption performance of spherical mesoporous alumina and the electrochemical performance of supported SnO<sub>2</sub> were also evaluated.

## 2. Results and Discussion

**Synthesis of mesoporous alumina spheres.** The synthesis of spherical macroporous alumina materials was achieved through the hydrothermal method, using hydrated alumina (AlOOH) as the precursor, along with chitin and P123 as the templates, and urea as a precipitant, while adapting the evaporation-induced self-assembly (EISA) method, as depicted in Figure 1. By systematically varying the reaction conditions, the impact of reaction temperature and time, as well as the chitin/P123 weight ratio, on the morphology and properties of the resulting spherical mesoporous alumina materials was investigated. The detailed process parameters are shown in the following table. During the calcining process at 700 °C, the organic components, including chitin and P123, underwent decomposition and evaporation, creating voids within the alumina matrix. This decomposition and evaporation of organic materials resulted in the formation of well-defined mesopores within the macroporous alumina microspheres.

**The effect of synthesis temperature and time on the morphology of spherical mesoporous alumina.** Figure 2a displays the X-ray diffraction (XRD) map of the precursor synthesized under various temperatures and durations. The precursors of R<sub>2:1</sub>T<sub>120</sub>H<sub>3</sub> and R<sub>0:1</sub>T<sub>120</sub>H<sub>9</sub> are primarily amorphous products. However, as the synthesis temperature increases to 160 °C and 180 °C, the precursors of R<sub>0:4</sub>T<sub>160</sub>H<sub>3</sub> and R<sub>3:1</sub>T<sub>180</sub>H<sub>3</sub> start to crystallize and become AlOOH (JCPDS 01-072-0359). This finding suggests that the synthesis temperature has a significant impact on the crystallization of the precursor. At lower hydrothermal temperatures, the system energy is insufficient to facilitate the formation and transformation of crystals, leading to the amorphous state of the samples. In contrast, when

the hydrothermal temperature increases, individual diffraction peaks emerge, and their intensity and width grow, indicating the increased crystallinity of the particles. The precursors of  $R_{3:1}T_{140}H_9$  and  $R_{1:1}T_{140}H_{15}$  are synthesized at  $140\text{ }^\circ\text{C}$  for 9 h and 15 h, respectively, providing sufficient energy for crystallization. Nevertheless, the diffraction peak intensity and width of the precursors of  $R_{3:1}T_{140}H_9$  and  $R_{1:1}T_{140}H_{15}$  are smaller compared with those of the precursors of  $R_{0:4}T_{160}H_3$  and  $R_{3:1}T_{180}H_3$  synthesized at higher temperatures. This difference implies that the crystallinity of particles in the precursors of  $R_{3:1}T_{140}H_9$  and  $R_{1:1}T_{140}H_{15}$  is weaker than that in the precursors of  $R_{0:4}T_{160}H_3$  and  $R_{3:1}T_{180}H_3$ . By controlling the growth rate of the crystal faces, the crystal orientation can be influenced, enabling control over the morphology and crystal structure of products.

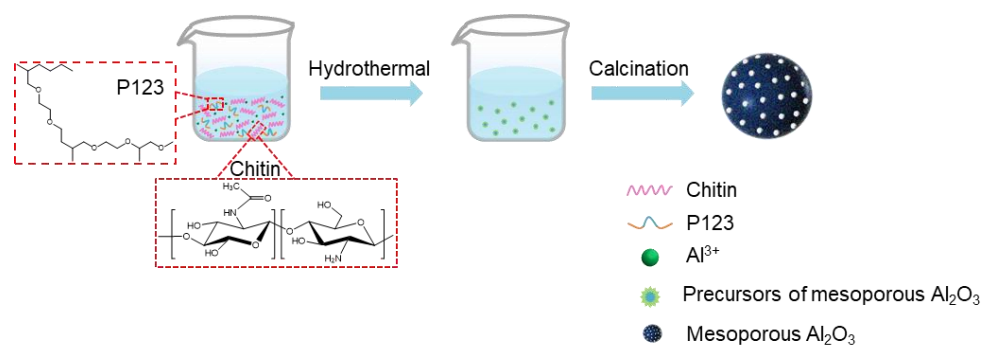


**Figure 1.** Schematic diagram of the preparation of spherical mesoporous alumina materials.

$\gamma\text{-Al}_2\text{O}_3$  belongs to the transitional form of alumina, and the random distribution of Al atoms results in a certain broadening of the XRD diffraction peak of  $\gamma\text{-Al}_2\text{O}_3$ . Figure 2b shows the mesoporous alumina XRD image after calcination at  $600\text{ }^\circ\text{C}$ . The amorphous precursor of  $R_{2:1}T_{120}H_3$  and  $R_{0:1}T_{120}H_9$  prepared at a lower synthesis temperature transforms into  $\gamma\text{-Al}_2\text{O}_3$  under calcination at  $700\text{ }^\circ\text{C}$ ; samples  $R_{0:4}T_{160}H_3$ ,  $R_{3:1}T_{180}H_3$ ,  $R_{3:1}T_{140}H_9$ , and  $R_{1:1}T_{140}H_{15}$  are  $\gamma\text{-Al}_2\text{O}_3$  (JCDPS 10-0425). With the increase in hydrothermal temperature, the position of each diffraction peak remains the same. However, the intensity and width of the diffraction peak grow larger, indicating an increase in the crystallinity of particles.

Figure 2c,d illustrates the SEM images of the mesoporous alumina samples prepared under different synthesis conditions. The images reveal that the temperature significantly influences the sample morphology, and  $140\text{ }^\circ\text{C}$  promotes the formation of spherical particles. When synthesized at  $120\text{ }^\circ\text{C}$ , the sample particles are massive and spherical (Figure 2c), while at  $140\text{ }^\circ\text{C}$ , the particles are regularly spherical with a smooth surface and particle sizes ranging between 50 nm and 200 nm (Figure 2d). As the synthesis temperature increases, more particles begin to crystallize and form crystalline solids. While these solids can completely transform into  $\gamma\text{-Al}_2\text{O}_3$  at  $700\text{ }^\circ\text{C}$ , the amorphous precursor requires more energy to undergo phase transformation at this temperature. Thus, crystallization is relatively slow, which favors the preparation of spherical mesoporous alumina (Figure 2a,b). However, at higher synthesis temperatures, the chitin powder used as a template tends to carbonize and lose some of its templating function. As a result, the sample transforms into irregular and flocculent particles that agglomerate (Figure S1a–d). Moreover, longer synthesis times are also not conducive to the development of spherical alumina particles (Figure S1c,d). Such conditions promote the development of flocculent, strip, and irregular particles, which hinder the normal growth of spherical particles.

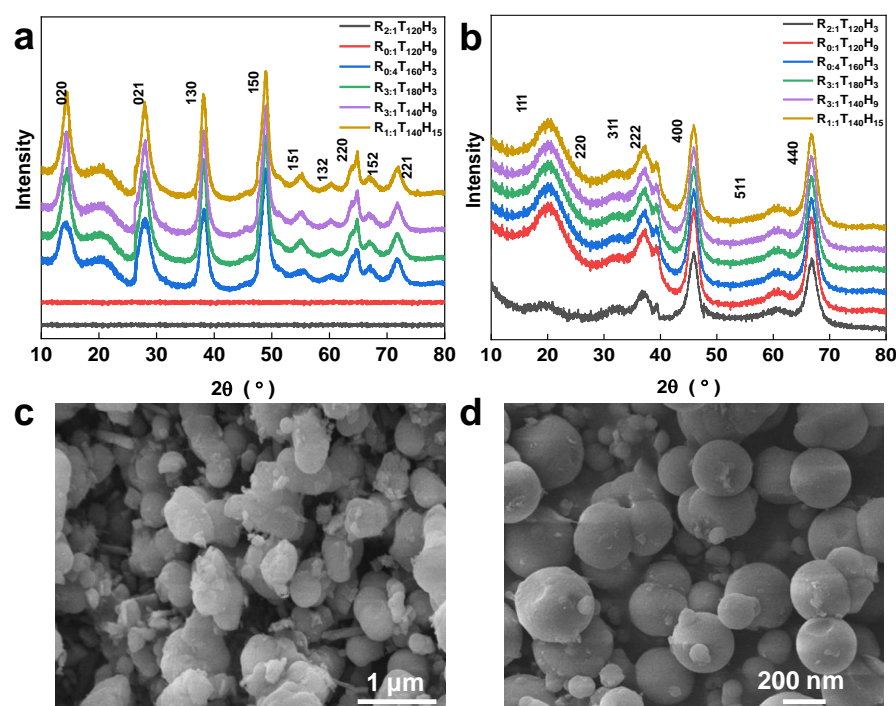


**Figure 2.** The X-ray diffraction (XRD) patterns of (a) the precursor and (b) mesoporous alumina XRD image under different synthesis conditions. The SEM images of mesoporous alumina under different synthesis conditions: (c) 120 °C, (d) 140 °C.

**The effect of chitin/P123 weight ratio on spherical morphology.** During the synthesis process, the amount of additive used has a significant impact on the morphology and structure of the final product [35–38]. Figure 3 displays the test results of spherical mesoporous alumina prepared using different chitin/P123 weight ratios (chitin quality:P123 quality).

When the chitin/P123 weight ratio is 0 ( $R = 0:4$ ), the predominant types of pores observed in the samples are ink-bottle-type pores with a large opening and small diameter, as well as uneven crack-like pores, as shown in Figure 3a. The nitrogen adsorption isotherm (see Figure 3f) exhibits a type IV curve with a hysteresis loop between H2 and H3 in the middle to high voltage range of  $0.5 p/p^0$  to  $0.9 p/p^0$ . The adsorption amount in this range is limited to only 0.4 to 1 mmol/g. This is primarily due to the irregular stacking of the strip-shaped samples, which results in a low number of mesoporous structures being distributed. As shown in Figure 3g, the pore sizes are mainly distributed in the range of approximately 7 nm.

As the weight ratio increases to 3, 4 ( $R = 3:1, 4:1$ ), the particle size of the sample becomes larger and the spherical shape becomes more regular (see Figure 3d,e). The nitrogen adsorption isotherms show that in the middle–high pressure area, the nitrogen adsorption capacity has further increased to about 7–8 mmol/g, as shown in Figure 3f,g. The pore size has further increased to about 9.4 nm and the pore volume has increased to  $0.7 \text{ cm}^3/\text{g}$ . The type IV curve of nitrogen adsorption isotherms shows a hysteresis loop between types H1 and H2. The formation of ink-bottle pores becomes more prominent, and the mesoporous structure becomes more developed. However, with the further increase in the weight ratio, the nitrogen adsorption capacity gradually decreases, indicating that excessive chitin may hinder the formation of the mesoporous structure. Therefore, the optimal weight ratio of chitin/P123 is 3, 4 ( $R = 3:1, 4:1$ ).

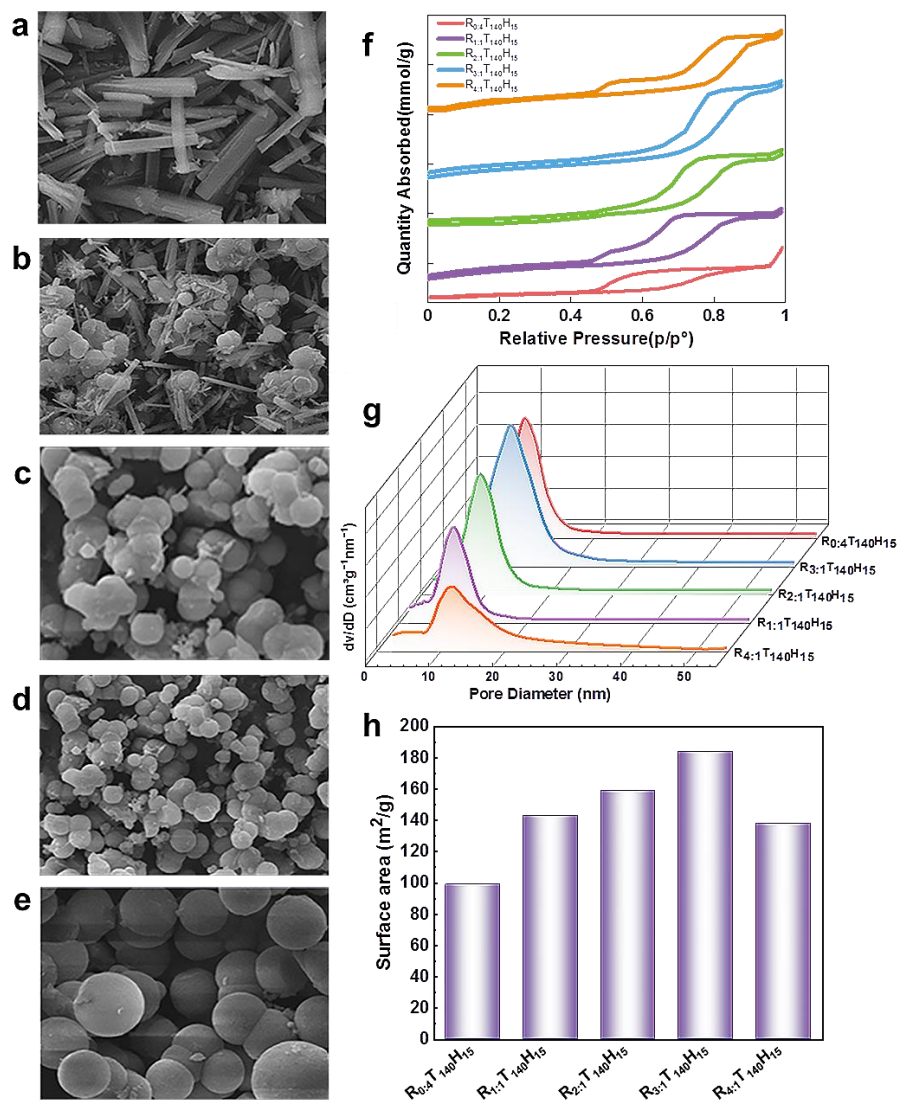


**Figure 3.** SEM images of (a)  $R_{0.4}T_{140}H_{15}$ , (b)  $R_{1.1}T_{140}H_{15}$ , (c)  $R_{2.1}T_{140}H_{15}$ , (d)  $R_{3.1}T_{140}H_{15}$ , and (e)  $R_{4.1}T_{140}H_{15}$ , (f) nitrogen sorption isotherms curves, (g) corresponding pore size distributions curves and (h) surface area histogram of as-prepared samples.

As shown in Figure 3d, at a weight ratio of 3 ( $R = 3:1$ ), the sample formed regular, uniform, and monodisperse microspheres and the predominant pore structure is a regular cylindrical shape with uniform size and shape. The nitrogen adsorption isotherms for this sample show a steep type IV curve and an H1 hysteresis loop (see Figure 3f), indicating that the sample has a uniform mesoporous structure and pore sizes are mainly distributed between 7 nm and 9 nm. Notably, the pore size has increased by 8.6 nm compared with the previous weight ratio, and the pore volume has also increased by  $0.3 \text{ cm}^3/\text{g}$ .

In summary, the chitin/P123 weight ratio has a significant effect on the morphology and structure of the mesoporous alumina sample. When the weight ratio is 0 ( $R = 0:4$ ), the sample has irregular strips with few mesoporous structures. As the weight ratio increases to 3 ( $R = 3:1$ ), the sample forms regular and uniform microspheres with a uniform mesoporous structure, which leads to increases in pore size, pore volume, and BET surface area. However, when the weight ratio is further increased to 4 ( $R = 4:1$ ), the sample exhibits adhesion and aggregation, and the pore size, pore volume, and BET surface area decrease. This is due to the increase in viscosity of the solution, which affects the template space steric effect and weakens homogeneous nucleation.

Using this method, this experiment involved successfully preparing spherical mesoporous alumina with uniform pore size, good dispersion, and identical morphology, with a chitin/P123 weight ratio of 3 ( $R = 3:1$ ). The amorphous precursor was prepared at a lower temperature of 140 °C and for a shorter time of 3 h. Upon calcination at 600 °C, inorganic  $Al^{3+}$  interacted slowly with and connected to the organic micelle interface via electrostatic interaction. This process allowed the aluminum ions to cover the entire particle surface and achieve consistent growth rates for all surfaces, ultimately resulting in the formation of spherical particles via homogeneous nucleation. The particle surface also formed a uniform mesoporous layer, resulting in the complete transformation of the precursor into spherical mesoporous  $Al_2O_3$ , as shown in Figure S2.

Figure S2 displays TEM images of spherical mesoporous alumina materials. The images clearly show that the alumina has a uniform and regular spherical form, as well as good dispersion. A 10 nm mesoporous layer uniformly covers the surface of the alumina particles, and the mesopore size is consistent throughout. The nitrogen sorption isotherms and corresponding pore size distributions of the spherical mesoporous alumina materials are also presented in Figure S2.

**CO<sub>2</sub> adsorption on spherical mesoporous alumina.** Figure 4a displays the CO<sub>2</sub> gas adsorption isotherm curves of spherical mesoporous alumina, which was synthesized with varying mass ratios of chitin to P123 at a temperature of 273 K [39–42]. With its large specific surface area and pore volume, spherical mesoporous alumina exhibits a high potential for gas adsorption. In this study, we investigated the adsorption capacity of spherical mesoporous alumina, synthesized with different ratios of template agents (chitin/P123), for carbon dioxide at 273 K.

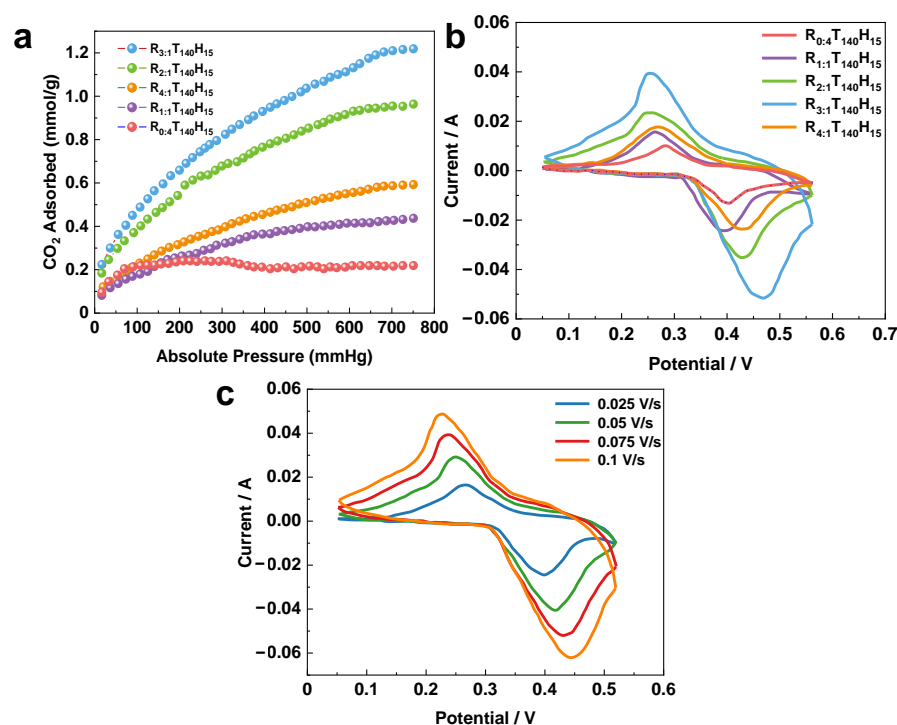


**Figure 4.** (a) CO<sub>2</sub>-adsorption isotherms of mesoporous alumina spheres synthesized with different templating agent ratios. Cyclic voltammograms of (b) different templating agent ratios and (c) different scan rates.

The adsorption capacity of CO<sub>2</sub> is highest (1.21 mmol/g) when the ratio of template agents is 3, resulting in the preparation of spherical mesoporous alumina with excellent dispersion and uniform pore size. Notably, the different mass ratios of template agents used in the synthesis produced alumina with distinct shapes, which significantly impacted their adsorption capacities.

**Electrochemical performance of porous alumina-supported SnO<sub>2</sub>.** The electrochemical performance of porous alumina-supported SnO<sub>2</sub> was studied using spherical mesoporous alumina-supported SnO<sub>2</sub> particle electrodes [43,44]. The electrodes were prepared using a dip-calcination method, with a loading amount of 4%. Cyclic voltammetry tests were carried out using a three-electrode system with 5 mol/L KOH solution as the electrolyte, a mercury/mercury oxide electrode as the reference electrode, and a platinum electrode as the auxiliary electrode. The prepared electrode sheet was used as the working electrode.

The CV curves of spherical mesoporous alumina-supported SnO<sub>2</sub> prepared with different ratios of template agents (chitin/P123) at a scan rate of 0.075 V/s are shown in Figure 4b. The redox peak in Figure 4b indicates the pseudocapacitive properties of the material. It was observed that when the ratio of the template agent increases, the area of the cyclic voltammetry curve increases, and the specific capacitance increases significantly, indicating that the spherical mesoporous alumina has a better energy storage performance. However, when the ratio of the template agent is too large (R = 4:1), the viscosity of the solution increases significantly. This increase in viscosity can affect the steric effect of the template space and weaken the homogeneous nucleation, which can lead to poor dispersion of particles. Poor particle dispersion can result in a poor carrier effect, which can negatively impact the electrochemical performance of the material.

The CV curves at different scan rates when the ratio of the template agent (chitin/P123) is 3 and the loading of SnO<sub>2</sub> is 4% are shown in Figure 4c. The CV curves were observed to be different with different scan rates, and with the increase in the test scan rate, the area of the closed graph also increased. This can be attributed to the high surface area and porous structure of the alumina support, which provides a large number of active sites for SnO<sub>2</sub> deposition and enhances the catalytic activity of SnO<sub>2</sub>. Mesoporous alumina spheres can be an excellent electrocatalyst support due to their special mesoporous structure.

**Periodic density functional theory (DFT).** To gain deep insight on CO<sub>2</sub> adsorption, we performed periodic density functional theory (DFT) calculations (see Supplemental Information for computational details) [45–49]. The (110) and (100) surfaces of  $\gamma$ -Al<sub>2</sub>O<sub>3</sub> were selected, as these two surfaces are predominant in  $\gamma$ -Al<sub>2</sub>O<sub>3</sub>, as proved with XRD in Figure 2b. The optimized structures of Al<sub>2</sub>O<sub>3</sub>(110) and Al<sub>2</sub>O<sub>3</sub>(100) surfaces are shown in Figure S3 [50–57]. The bare Al<sub>2</sub>O<sub>3</sub>(110) surface is terminated with two-coordinated O<sub>(II)</sub>, three-coordinated O<sub>(III)</sub>, and four-coordinated Al<sub>(IV)</sub>, while the Al<sub>2</sub>O<sub>3</sub>(100) surface is exposed with three-coordinated O<sub>(III)</sub> and five-coordinated Al<sub>(V)</sub>. Our results indicate that the surface energy of Al<sub>2</sub>O<sub>3</sub>(110) is lower than that of Al<sub>2</sub>O<sub>3</sub>(100) (1.41 J·m<sup>-2</sup> vs. 2.45 J·m<sup>-2</sup>), indicating that the Al<sub>2</sub>O<sub>3</sub>(110) surface is more stable [58–60].

The adsorption energies and optimized structures of CO<sub>2</sub> on Al<sub>2</sub>O<sub>3</sub>(110) and Al<sub>2</sub>O<sub>3</sub>(100) surfaces are shown in Figure 5 and Figure S4 [61]. The DFT calculated results show that the formation of carbonate species is the most stable adsorption model, where CO<sub>2</sub> binds in an ambidentate configuration across the O-Al bridge sites with adsorption energies of -0.93 eV and -0.75 eV on Al<sub>2</sub>O<sub>3</sub>(110) and Al<sub>2</sub>O<sub>3</sub>(100), respectively. To obtain insight into the nature of molecular adsorption behavior, the differences in charge density ( $\Delta\rho$ ) of the most stable adsorption CO<sub>2</sub> on Al<sub>2</sub>O<sub>3</sub> surfaces were calculated. The results are clearly plotted in Figure 5. It is evident that charges accumulate and deplete around the O and C of CO<sub>2</sub> on both surfaces, respectively. The net result is the transfer of electrons from Al<sub>2</sub>O<sub>3</sub> surfaces to the adsorbed CO<sub>2</sub>. The Bader charge analyses proved that the electronic charges transferred from the Al<sub>2</sub>O<sub>3</sub>(110) and Al<sub>2</sub>O<sub>3</sub>(100) surfaces to CO<sub>2</sub> are 0.28 a.u. and 0.29 a.u., respectively. These two surfaces achieve the purpose of CO<sub>2</sub> activation by transferring their electrons to the antibonding molecular orbital of CO<sub>2</sub>. The former is more stable, mainly because there are more electrons near the Fermi level on the atoms of the surface active site of Al<sub>(IV)</sub>-O<sub>(II)</sub> on Al<sub>2</sub>O<sub>3</sub>(110) than that of Al<sub>(V)</sub>-O<sub>(III)</sub> on Al<sub>2</sub>O<sub>3</sub>(100) (see projected density of states in Figure S5). The above results demonstrate that both surfaces can strongly adsorb CO<sub>2</sub>, which explains the experimental results. The difference in the amount of CO<sub>2</sub> adsorbed by Al<sub>2</sub>O<sub>3</sub> synthesized under different conditions

is mainly due to the different surface areas, which give different numbers of exposed active sites. The higher the crystallinity, the higher the surface content of Al<sub>2</sub>O<sub>3</sub>(110) [45].

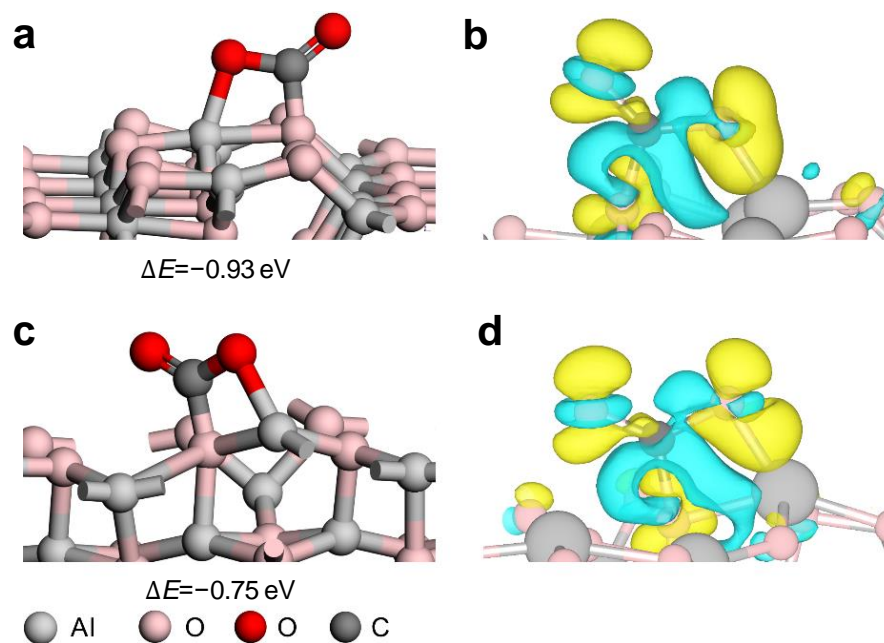


**Figure 5.** The adsorption energies and optimized structures of CO<sub>2</sub> on (a) Al<sub>2</sub>O<sub>3</sub>(110) and (b) Al<sub>2</sub>O<sub>3</sub>(100) surfaces. (c,d) are the charge differences in CO<sub>2</sub> adsorption on Al<sub>2</sub>O<sub>3</sub>(110) and Al<sub>2</sub>O<sub>3</sub>(100) surfaces, respectively. The values of the isosurfaces are  $\pm 0.003 \text{ e}/\text{\AA}^3$ . Yellow and light cyan isosurfaces indicate the accumulation and depletion of charge density.

### 3. Materials and Methods

#### 3.1. Synthesis of Mesoporous Alumina Spheres

The typical synthesis process involves the following steps: Firstly, 6.6 g of hydrated alumina is added to ultrapure water with a resistivity of 18 M $\Omega$ ·cm, and dissolved in a volumetric flask to prepare a 0.6 mol/L hydrated alumina solution. Subsequently, 3 g of chitin and 1 g of P123 are dissolved in 40 mL of isopropanol, followed by the addition of 2.4 g of urea, and stirred until fully dissolved. Next, 30 mL of the prepared hydrated alumina solution is added and vigorously stirred at room temperature. After 30 min, the solution is transferred into an autoclave with a PTFE liner, and reacted at 140 °C for 3 h. Following this, the product is rapidly cooled to room temperature using a water bath. The synthesized samples are purified via repeated redispersion in ultrapure water followed by filtration to remove any unreacted reagents. The samples are washed with 500 mL of ultrapure water and 200 mL of absolute ethanol, respectively, 3–5 times. The obtained material is then dried under vacuum at 80 °C, and finally calcined at 700 °C for 2 h. The resulting product is a white spherical mesoporous alumina powder.

The hydrothermal reaction temperatures are 120 °C, 140 °C, 160 °C, and 180 °C. The hydrothermal reaction times are 3 h, 9 h, and 15 h. The chitin/P123 weight ratio is maintained in the range of 0–4. Table 1 shows the process parameters for preparing alumina and spherical mesoporous alumina, respectively. The resultant samples were denoted as R<sub>m</sub>T<sub>n</sub>H<sub>s</sub> (m = chitin/P123 weight ratio, n (reaction temperature) = 120, 140, 160, or 180 °C, respectively; s (reaction time) = 3, 9, or 15 h, respectively).

**Table 1.** Detailed process parameters for preparing spherical mesoporous alumina.

Sample	Weight Ratio (Chitin/P123)	Reaction Temperature (°C)	Reaction Time (h)
R <sub>2:1</sub> T <sub>120</sub> H <sub>3</sub>	2:1	120	3
R <sub>0:1</sub> T <sub>120</sub> H <sub>9</sub>	0:1	120	9
R <sub>4:1</sub> T <sub>120</sub> H <sub>15</sub>	4:1	120	15
R <sub>1:2</sub> T <sub>140</sub> H <sub>3</sub>	1:2	140	3
R <sub>3:1</sub> T <sub>140</sub> H <sub>9</sub>	3:1	140	9
R <sub>1:1</sub> T <sub>140</sub> H <sub>15</sub>	1:1	140	15
R <sub>0:4</sub> T <sub>160</sub> H <sub>3</sub>	0:4	160	3
R <sub>2:3</sub> T <sub>160</sub> H <sub>9</sub>	2:3	160	9
R <sub>3:1</sub> T <sub>160</sub> H <sub>15</sub>	3:1	160	15
R <sub>3:1</sub> T <sub>180</sub> H <sub>3</sub>	3:1	180	3
R <sub>1:2</sub> T <sub>180</sub> H <sub>9</sub>	1:2	180	9
R <sub>0:4</sub> T <sub>180</sub> H <sub>15</sub>	0:4	180	15

### 3.2. Physical Characterization

The physical properties of the synthesized spherical mesoporous alumina materials were determined using various techniques. The X-ray diffraction (XRD) patterns were obtained using a PANalytical X'Pert PRO diffractometer with Cu K $\alpha$  radiation ( $\lambda = 1.54056 \text{ \AA}$ ) over the  $2\theta$  range of  $10\text{--}80^\circ$ . The N<sub>2</sub> adsorption–desorption isotherms were measured at  $-196^\circ\text{C}$  using a Micromeritics Tristars 3000 analyzer. The CO<sub>2</sub> adsorption isotherms of the synthesized spherical mesoporous alumina materials were measured using a Micromeritics Tristars 3000 analyzer instrument at  $25^\circ\text{C}$ . Prior to the measurements, the samples were degassed at  $180^\circ\text{C}$  under vacuum for 6 h to remove any moisture and adsorbed gases. The CO<sub>2</sub>-adsorption isotherms were obtained at various pressures ranging from 0 to 1 bar. The CO<sub>2</sub> uptake capacity of the materials was calculated from the amount of gas adsorbed at equilibrium and the mass of the sample. The specific surface area (SSA) and pore volume were calculated using the Brunauer–Emmett–Teller (BET) method and Barrett–Joyner–Halenda (BJH) analysis, respectively. The scanning electron microscopy (SEM) images were obtained using a KYKY-2800B microscope. Transmission electron microscopy (TEM) measurements were carried out on Tecnai G2 F20 operated at 200 kV.

### 3.3. Electrochemistry Characterization

The electrochemical performance of the synthesized spherical mesoporous alumina materials was evaluated using a three-electrode system with a platinum wire as the counter electrode, a mercury/mercury oxide electrode as the reference electrode, and the synthesized material as the working electrode. The electrochemical tests were carried out using a CHI660D electrochemical workstation in a 5 mol/L KOH electrolyte solution. Cyclic voltammetry (CV) was carried out in the potential range of 0 to 0.7 V vs. Hg/HgO at a scan rate of 0.025–0.1 V/s to investigate the electrochemical stability of the synthesized materials.

## 4. Conclusions

In summary, using P123 as a soft template, mesoporous alumina spheres with high specific surface area, larger pore size, and larger pore volume were synthesized. The synthesis conditions, such as temperature, time, and the weight ratio of additives, have a significant impact on the morphology and properties of the material. By optimizing these conditions, monodisperse spherical shape and uniform mesoporous structure can be elicited, leading to better CO<sub>2</sub> adsorption capacity and improved electrocatalytic effect. This method provides a new way to control pore size and structure, and the material has potential applications in various fields. The periodic density functional theory (DFT) calculation results demonstrate that both the (110) and (100) surfaces of  $\gamma\text{-Al}_2\text{O}_3$  can strongly adsorb CO<sub>2</sub>, which explains the experimental results. The difference in the amount of CO<sub>2</sub> adsorbed by Al<sub>2</sub>O<sub>3</sub> synthesized under different conditions is mainly due to the

different surface areas, which give different numbers of exposed active sites. The higher the crystallinity, the higher the surface content of Al<sub>2</sub>O<sub>3</sub>(110). This research contributes to the development of mesoporous materials and enriches the diversity in solution phase synthetic chemistry.

**Supplementary Materials:** The following supporting information can be downloaded at: <https://www.mdpi.com/article/10.3390/molecules28155622/s1>, Table S1: Process parameters of alumina prepared by different reaction temperature and reaction time; Table S2: Process parameters of spherical alumina prepared by different addition of Chitin powder; Table S3: Textural properties of mesoporous alumina with different Chitin:P123 weight ratio; Figure S1: Mesoporous alumina samples SEM image prepared under different synthesis conditions: a: Al<sub>2</sub>O<sub>3</sub>-160-3; b: Al<sub>2</sub>O<sub>3</sub>-180-3; c: Al<sub>2</sub>O<sub>3</sub>-140-6; d: Al<sub>2</sub>O<sub>3</sub>-140-9; Figure S2: TEM images of spherical mesoporous alumina materials; Figure S3: The top view and side view of the computational models. (a) Al<sub>2</sub>O<sub>3</sub>(110) and (b) Al<sub>2</sub>O<sub>3</sub>(100) surfaces; Figure S4: The adsorption energies and optimized structures of CO<sub>2</sub> on (a)-(b) Al<sub>2</sub>O<sub>3</sub>(110) and (c) Al<sub>2</sub>O<sub>3</sub>(100) surfaces; Figure S5: Projected density of states (PDOS) of the active sites of Al(IV)-O(II) or Al(V)-O(III) on Al<sub>2</sub>O<sub>3</sub>(110) and Al<sub>2</sub>O<sub>3</sub>(100), respectively. Reference citations of [45–61].

**Author Contributions:** Y.X., L.Z. and X.T. conceived the project. Y.X., L.Z., Y.H. and X.T. supervised the project. Y.X., L.G. and M.X. carried out the material growth experiment and performed the electrochemical and CO<sub>2</sub> adsorption measurements. Y.X., L.G., M.X. and B.Y. conducted SEM, TEM, nitrogen sorption, and XRD characterizations. All authors contributed to the scientific discussion and writing of the manuscript. All authors have read and agreed to the published version of the manuscript.

**Funding:** This research was funded by the National Natural Science Foundation of China (No. 52062005 and No. 52074141), the Key Science and Technology Support Project of Guizhou Province (No. [2021]326), Guizhou Provincial Key Laboratory in the Higher Education Institutions of Low-Dimensional Materials and Environmental and Ecological Governance (No. [2022]046), and the Department of Education of Guizhou Province Natural Science Projects (No. 2022[161]).

**Institutional Review Board Statement:** Not applicable.

**Informed Consent Statement:** Informed consent was obtained from all subjects involved in this study.

**Data Availability Statement:** Data sharing not applicable. No new data were created or analyzed in this study.

**Conflicts of Interest:** The authors declare no conflict of interest.

## References

1. Zhang, H.; Shan, G.; Liu, H.; Xing, J. Preparation of (Ni/W)-gamma-Al<sub>2</sub>O<sub>3</sub> microspheres and their application in adsorption desulfurization for model gasoline. *Chem. Eng. Commun.* **2007**, *194*, 938–945. [\[CrossRef\]](#)
2. Al-Ghouti, M.A.; Khan, M.; Malik, A.; Khraisheh, M.; Hijazi, D.; Mohamed, S.; Alsorour, S.; Eltayeb, R.; Al Mahmoud, F.; Alahmad, J. Development of novel nano-γ-Al<sub>2</sub>O<sub>3</sub> adsorbent from waste aluminum foil for the removal of boron and bromide from aqueous solution. *J. Water Process. Eng.* **2022**, *50*, 103312. [\[CrossRef\]](#)
3. Shen, X.; Yan, F.; Li, C.; Qu, F.; Wang, Y.; Zhang, Z. Biogas upgrading via cyclic CO<sub>2</sub> adsorption: Application of highly regenerable PEI@ nano-Al<sub>2</sub>O<sub>3</sub> adsorbents with anti-urea properties. *Environ. Sci. Technol.* **2021**, *55*, 5236–5247. [\[CrossRef\]](#)
4. Bartsch, M.; Saruhan, B.; Schmücker, M.; Schneider, H. Novel low-temperature processing route of dense mullite ceramics by reaction sintering of amorphous SiO<sub>2</sub>-coated gamma-Al<sub>2</sub>O<sub>3</sub> particle nanocomposites. *J. Am. Ceram. Soc.* **2004**, *82*, 1388–1392. [\[CrossRef\]](#)
5. Liu, X.; Zou, B.; Xing, H.; Huang, C. The preparation of ZrO<sub>2</sub>-Al<sub>2</sub>O<sub>3</sub> composite ceramic by SLA-3D printing and sintering processing. *Ceram. Int.* **2020**, *46*, 937–944. [\[CrossRef\]](#)
6. Lietti, L.; Forzatti, P.; Nova, I.; Tronconi, E. NO<sub>x</sub> storage reduction over Pt-Ba/gamma-Al<sub>2</sub>O<sub>3</sub> catalyst. *J. Catal.* **2001**, *204*, 175–191. [\[CrossRef\]](#)
7. Shumilov, V.; Kirilin, A.; Tokarev, A.; Boden, S.; Schubert, M.; Hampel, U.; Hupa, L.; Salmi, T.; Murzin, D.Y. Preparation of γ-Al<sub>2</sub>O<sub>3</sub>/α-Al<sub>2</sub>O<sub>3</sub> ceramic foams as catalyst carriers via the replica technique. *Catal. Today* **2022**, *383*, 64–73. [\[CrossRef\]](#)
8. Zhao, J.; Zhang, G.; Liu, H.; Shu, Q.; Zhang, Q. Improved charge transfer and morphology on Ti-modified Cu/γ-Al<sub>2</sub>O<sub>3</sub>/Al catalyst enhance the activity for methanol steam reforming. *Int. J. Hydrogen Energy* **2022**, *47*, 18294–18304. [\[CrossRef\]](#)

9. Wang, C.; Zhang, Q.; Yan, B.; You, B.; Zheng, J.; Feng, L.; Zhang, C.; Jiang, S.; Chen, W.; He, S. Facet Engineering of Advanced Electrocatalysts Toward Hydrogen/Oxygen Evolution Reactions. *Nano-Micro Lett.* **2023**, *15*, 52. [\[CrossRef\]](#)
10. Fereja, S.L.; Li, P.; Zhang, Z.; Guo, J.; Fang, Z.; Li, Z.; He, S.; Chen, W. W-doping induced abundant active sites in a 3D NiS<sub>2</sub>/MoO<sub>2</sub> heterostructure as an efficient electrocatalyst for urea oxidation and hydrogen evolution reaction. *Chem. Eng. J.* **2022**, *432*, 134274–134280. [\[CrossRef\]](#)
11. Du, C.; Li, P.; Zhuang, Z.; Fang, Z.; He, S.; Feng, L.; Chen, W. Highly porous nanostructures: Rational fabrication and promising application in energy electrocatalysis. *Coord. Chem. Rev.* **2022**, *466*, 214604. [\[CrossRef\]](#)
12. Wang, C.; Yan, B.; Chen, Z.; You, B.; Liao, T.; Zhang, Q.; Lu, Y.; Jiang, S.; He, S. Recent advances in carbon substrate supported nonprecious nanoarrays for electrocatalytic oxygen evolution. *J. Mater. Chem. A* **2021**, *9*, 25773–25795. [\[CrossRef\]](#)
13. Kim, K.T.; Dao, T.D.; Jeong, H.M.; Anjanapura, R.V.; Aminabhavi, T.M. Graphene coated with alumina and its utilization as a thermal conductivity enhancer for alumina sphere/thermoplastic polyurethane composite. *Mater. Chem. Phys.* **2015**, *153*, 291–300. [\[CrossRef\]](#)
14. Hosseini, S.A.; Niaei, A.; Salari, D. Production of  $\gamma$ -Al<sub>2</sub>O<sub>3</sub> from Kaolin. *Open J. Phys. Chem.* **2015**, *01*, 23–27. [\[CrossRef\]](#)
15. Dabbagh, H.A.; Shahraki, M. Mesoporous nano rod-like  $\gamma$ -alumina synthesis using phenol-formaldehyde resin as a template. *Microporous Mesoporous Mater.* **2013**, *175*, 8–15. [\[CrossRef\]](#)
16. Feng, J.T.; Lin, J.; Li, F.; Evans, D.G.; Li, D.Q. Preparation, structure and properties of micro-spherical alumina with magnetic spinel ferrite cores. *Appl. Catal. A Gen.* **2007**, *329*, 112–119. [\[CrossRef\]](#)
17. Lv, Y.; Li, D.; Tang, P.; Feng, Y. A simple and promoter free way to synthesize spherical  $\gamma$ -alumina with high hydrothermal stability. *Mater. Lett.* **2015**, *155*, 75–77. [\[CrossRef\]](#)
18. Wu, Q.; Zhang, F.; Yang, J.; Li, Q.; Tu, B.; Zhao, D. Synthesis of ordered mesoporous alumina with large pore sizes and hierarchical structure. *Microporous Mesoporous Mater.* **2011**, *143*, 406–412. [\[CrossRef\]](#)
19. Tanaka, K.; Imai, T.; Murakami, Y.; Matsumoto, T.; Sugimoto, W.; Takasu, Y. Microporous structure of alumina prepared by a salt catalytic sol-gel process. *Chem. Lett.* **2002**, *31*, 110–111. [\[CrossRef\]](#)
20. Yan, B.; Zheng, J.; Feng, L.; Zhang, Q.; Zhang, C.; Ding, Y.; Han, J.; Jiang, S.; He, S. Pore engineering: Structure-capacitance correlations for biomass-derived porous carbon materials. *Mater. Des.* **2023**, *229*, 111904. [\[CrossRef\]](#)
21. Deng, W.; Xu, Y.; Zhang, X.; Li, C.; Liu, Y.; Xiang, K.; Chen, H. (NH<sub>4</sub>)<sub>2</sub>Co<sub>2</sub>V<sub>10</sub>O<sub>28</sub>·16H<sub>2</sub>O/(NH<sub>4</sub>)<sub>2</sub>V<sub>10</sub>O<sub>25</sub>·8H<sub>2</sub>O heterostructure as cathode for high-performance aqueous Zn-ion batteries. *J. Alloys Compd.* **2022**, *903*, 163824. [\[CrossRef\]](#)
22. Feng, L.; Yan, B.; Zheng, J.; Zhang, Q.; Wei, R.; Zhang, C.; Han, J.; Jiang, S.; He, S. Chemical foaming-assisted synthesis of N, O co-doped hierarchical porous carbon from soybean protein for high rate performance supercapacitors. *Diam. Relat. Mater.* **2023**, *133*, 109767. [\[CrossRef\]](#)
23. Dahlan, I.; Marsih, N.; Panpranot, J.  $\gamma$ -Alumina Nanotubes Prepared by Hydrothermal Method as Support of Iron, Cobalt and Nickel for Fischer-Tropsch Catalysts. *Chem. Mater. Res.* **2012**, *2*, 31–38.
24. Saeb, M.R.; Rabiee, N.; Seidi, F.; Far, B.F.; Bagherzadeh, M.; Lima, E.C.; Rabiee, M. Green CoNi<sub>2</sub>S<sub>4</sub>/porphyrin decorated carbon-based nanocomposites for genetic materials detection. *J. Bioresour. Bioprod.* **2021**, *6*, 215–222. [\[CrossRef\]](#)
25. Deeksha, B.; Sadanand, V.; Hariram, N.; Rajulu, A.V. Preparation and properties of cellulose nanocomposite fabrics with in situ generated silver nanoparticles by bioreduction method. *J. Bioresour. Bioprod.* **2021**, *6*, 75–81. [\[CrossRef\]](#)
26. He, M.; Wang, X.; Wang, Z.; Chen, L.; Lu, Y.; Zhang, X.; Li, M.; Liu, Z.; Zhang, Y.; Xia, H.; et al. Biocompatible and biodegradable bioplastics constructed from chitin via a “green” pathway for bone repair. *ACS Sustain. Chem. Eng.* **2017**, *5*, 9126–9135. [\[CrossRef\]](#)
27. Sun, G.; Zou, C.; Sun, W.; Fang, Y.; He, S.; Liu, Y.; Zhang, J.; Zhu, Y.; Wang, J. Structural reconstruction of BiPbO<sub>2</sub> Br nanosheets for electrochemical CO<sub>2</sub> reduction to formate. *Mater. Chem. Front.* **2023**. [\[CrossRef\]](#)
28. Chen, Z.; Chen, G.; Wang, C.; Chen, D.; Zhang, Q.; Jiang, L.; Zhang, C.; Liu, K.; He, S. Capacitive properties of carbon nanofibers derived from blends of cellulose acetate and polyacrylonitrile. *New J. Chem.* **2023**. [\[CrossRef\]](#)
29. Zheng, J.; Yan, B.; Feng, L.; Zhang, Q.; Han, J.; Zhang, C.; Yang, W.; Jiang, S.; He, S. Al Foil-Supported Carbon Nanosheets as Self-Supporting Electrodes for High Areal Capacitance Supercapacitors. *Molecules* **2023**, *28*, 1831. [\[CrossRef\]](#)
30. Soni, S.S.; Brotons, G.; Bellour, M.; Narayanan, T.; Gibaud, A. Quantitative SAXS analysis of the P123/water/ethanol ternary phase diagram. *J. Phys. Chem. B* **2006**, *110*, 15157–15165. [\[CrossRef\]](#)
31. Elma, M.; Wang, D.K.; Yacou, C.; da Costa, J.C.D. Interlayer-free P123 carbonised template silica membranes for desalination with reduced salt concentration polarisation. *J. Membr. Sci.* **2015**, *475*, 376–383. [\[CrossRef\]](#)
32. Jia, C.; Zhang, Y.; Kong, Q.; Wang, Q.; Chen, G.; Guam, H.; Dong, C. Soft-template synthesis of mesoporous NiFe<sub>2</sub>O<sub>4</sub> for highly sensitive acetone detection. *J. Mater. Sci. Mater. Electron.* **2020**, *31*, 6000–6007. [\[CrossRef\]](#)
33. Biriaei, R.; Nohair, B.; Kaliaguine, S. A facile route to synthesize mesoporous ZSM-5 with hexagonal arrays using P123 triblock copolymer. *Microporous Mesoporous Mater.* **2020**, *298*, 110067. [\[CrossRef\]](#)
34. Cabrera, S.; Haskouri, J.E.; Alamo, J.; Beltrán, A.; Beltrán, D.; Mendioroz, S.; Marcos, M.D.; Amorós, P. Surfactant-Assisted Synthesis of Mesoporous Alumina Showing Continuously Adjustable Pore Sizes. *Adv. Mater.* **1999**, *11*, 379–381. [\[CrossRef\]](#)
35. Zhi, C.; Shi, S.; Zhang, S.; Si, Y.; Yang, J.; Meng, S.; Fei, B.; Hu, J. Bioinspired All-Fibrous Directional Moisture-Wicking Electronic Skins for Biomechanical Energy Harvesting and All-Range Health Sensing. *Nano-Micro Lett.* **2023**, *15*, 60. [\[CrossRef\]](#)
36. Sikora, A.; Bednarz, Ł.; Fałat, T.; Wałęcki, M.; Adamowska, M. Investigation of the impact of simulated solar radiation on the micro- and nanoscale morphology and mechanical properties of a sheet moulded composite surface. *Mater. Sci-Poland* **2016**, *34*, 641–649. [\[CrossRef\]](#)

37. Shkoda, O.A. Study of the effect of the size of the initial nickel powder on the structure formation of the mixture during mechanical activation of titanium and nickel. *JPCS* **2020**, *1459*, 012021. [[CrossRef](#)]
38. Zou, Y.; Zhou, X.; Xie, L.; Tang, H.; Yan, F. Vertically-ordered mesoporous silica films grown on boron nitride-graphene composite modified electrodes for rapid and sensitive detection of carbendazim in real samples. *Front. Chem.* **2022**, *10*, 939510. [[CrossRef](#)]
39. Mohan, Y.M.; Vimala, K.; Thomas, V.; Varaprasad, K.; Sreedhar, B.; Bajpai, S.; Raju, K.M. Controlling of silver nanoparticles structure by hydrogel networks. *J. Colloid Interface Sci.* **2010**, *342*, 73–82. [[CrossRef](#)]
40. Li, Q.; Jiang, R.; Dou, Y.; Wu, Z.; Huang, T.; Feng, D.; Yang, J.; Yu, A.; Zhao, D. Synthesis of mesoporous carbon spheres with a hierarchical pore structure for the electrochemical double-layer capacitor. *Carbon* **2011**, *49*, 1248–1257. [[CrossRef](#)]
41. Xin, Y.; Jiang, P.; Yu, M.; Gu, H.; Li, Q.; Zhang, Z. A universal route to fabricate hierarchically ordered macro/mesoporous oxides with enhanced intrinsic activity. *J. Mater. Chem. A* **2014**, *2*, 6419–6425. [[CrossRef](#)]
42. Deng, W.N.; Li, Y.H.; Xu, D.F.; Zhou, W.; Xiang, K.X.; Chen, H. Three-dimensional hierarchically porous nitrogen-doped carbon from water hyacinth as selenium host for high-performance lithium–selenium batteries. *Rare Met.* **2022**, *41*, 3432–3445. [[CrossRef](#)]
43. Zhang, Q.; Yan, B.; Feng, L.; Zheng, J.; You, B.; Chen, J.; Zhao, X.; Zhang, C.; Jiang, S.; He, S. Progress in the use of organic potassium salts for the synthesis of porous carbon nanomaterials: Microstructure engineering for advanced supercapacitors. *Nanoscale* **2022**, *14*, 8216–8244. [[CrossRef](#)] [[PubMed](#)]
44. Yan, B.; Zheng, J.; Wang, F.; Zhao, L.; Zhang, Q.; Xu, W.; He, S. Review on porous carbon materials engineered by ZnO templates: Design, synthesis and capacitance performance. *Mater. Des.* **2021**, *201*, 109518. [[CrossRef](#)]
45. Digne, M.; Sautet, P.; Raybaud, P.; Euzen, P.; Toulhoat, H. Use of DFT to achieve a rational understanding of acid–basic properties of  $\gamma$ -alumina surfaces. *J. Catal.* **2004**, *226*, 54–68. [[CrossRef](#)]
46. Kresse, G.; Hafner, J. Ab initio molecular-dynamics simulation of the liquid-metal-amorphous-semiconductor transition in germanium. *Phys. Rev. B* **1994**, *49*, 14251–14269. [[CrossRef](#)]
47. Kresse, G.; Hafner, J. Ab initio molecular dynamics for open-shell transition metals. *Phys. Rev. B* **1993**, *48*, 13115–13118. [[CrossRef](#)]
48. Kresse, G.; Furthmüller, J. Efficiency of ab-initio total energy calculations for metals and semiconductors using a plane-wave basis set. *Comp. Mater. Sci.* **1996**, *6*, 15–50. [[CrossRef](#)]
49. Kresse, G.; Furthmüller, J. Efficient iterative schemes for ab initio total-energy calculations using a plane-wave basis set. *Phys. Rev. B* **1996**, *54*, 11169–11186. [[CrossRef](#)]
50. Kresse, G.; Joubert, D. From ultrasoft pseudopotentials to the projector augmented-wave method. *Phys. Rev. B* **1999**, *59*, 1758–1775. [[CrossRef](#)]
51. Kresse, G.; Hafner, J. Ab initio molecular dynamics for liquid metals. *Phys. Rev. B* **1993**, *47*, 558–561. [[CrossRef](#)]
52. Monkhorst, H.J.; Pack, J.D. Special points for Brillouin-zone integrations. *Phys. Rev. B* **1976**, *13*, 5188–5192. [[CrossRef](#)]
53. Gutiérrez, G.; Taga, A.; Johansson, B. Theoretical structure determination of  $\gamma$ -Al<sub>2</sub>O<sub>3</sub>. *Phys. Rev. B* **2001**, *65*, 012101. [[CrossRef](#)]
54. Pinto, H.P.; Nieminen, R.M.; Elliott, S.D. Ab initio study of  $\gamma$ -Al<sub>2</sub>O<sub>3</sub> surfaces. *Phys. Rev. B* **2004**, *70*, 125402. [[CrossRef](#)]
55. Krokidis, X.; Raybaud, P.; Gobichon, A.-E.; Rebours, B.; Euzen, P.; Toulhoat, H. Theoretical Study of the Dehydration Process of Boehmite to  $\gamma$ -Alumina. *J. Phys. Chem. B* **2001**, *105*, 5121–5130. [[CrossRef](#)]
56. Menéndez-Proupin, E.; Gutiérrez, G. Electronic properties of bulk  $\gamma$ -Al<sub>2</sub>O<sub>3</sub>. *Phys. Rev. B* **2005**, *72*, 035116. [[CrossRef](#)]
57. Ching, W.Y.; Ouyang, L.; Rulis, P.; Yao, H. Ab initio study of the physical properties of  $\gamma$ -Al<sub>2</sub>O<sub>3</sub>: Lattice dynamics, bulk properties, electronic structure, bonding, optical properties, and ELNES/XANES spectra. *Phys. Rev. B* **2008**, *78*, 014106. [[CrossRef](#)]
58. Ferreira, A.R.; Martins, M.J.F.; Konstantinova, E.; Capaz, R.B.; Souza, W.F.; Chiaro, S.S.X.; Leitão, A.A. Direct comparison between two  $\gamma$ -alumina structural models by DFT calculations. *J. Solid State Chem.* **2011**, *184*, 1105–1111. [[CrossRef](#)]
59. Dabbagh, H.A.; Taban, K.; Zamani, M. Effects of vacuum and calcination temperature on the structure, texture, reactivity, and selectivity of alumina: Experimental and DFT studies. *J. Mol. Catal. A Chem.* **2010**, *326*, 55–68. [[CrossRef](#)]
60. Ionescu, A.; Allouche, A.; Aycard, J.-P.; Rajzmann, M.; Hutschka, F. Study of  $\gamma$ -Alumina Surface Reactivity: Adsorption of Water and Hydrogen Sulfide on Octahedral Aluminum Sites. *J. Phys. Chem. B* **2002**, *106*, 9359–9366. [[CrossRef](#)]
61. Ionescu, A.; Allouche, A.; Aycard, J.-P.; Rajzmann, M.; Gall, R.L. Study of  $\gamma$ -Alumina-Supported Hydrotreating Catalyst: I. Adsorption of Bare MoS<sub>2</sub> Sheets on  $\gamma$ -Alumina Surfaces. *J. Phys. Chem. B* **2003**, *107*, 8490–8497. [[CrossRef](#)]

**Disclaimer/Publisher’s Note:** The statements, opinions and data contained in all publications are solely those of the individual author(s) and contributor(s) and not of MDPI and/or the editor(s). MDPI and/or the editor(s) disclaim responsibility for any injury to people or property resulting from any ideas, methods, instructions or products referred to in the content.